General Method for the Synthesis of Hierarchical Nanocrystal-Based Mesoporous Materials

Iris E. Rauda,[†] Raffaella Buonsanti,[‡] Laura C. Saldarriaga-Lopez,[†] Kanokraj Benjauthrit,[†] Laura T. Schelhas,[†] Morgan Stefik,[§,‖] Veronica Augustyn,[⊥] Jesse Ko,[⊥] Bruce Dunn,[⊥] Ulrich Wiesner,[§] Delia J. Milliron,[‡] and Sarah H. Tolbert[†,⊥,]*

[†]Department of Chemistry and Biochemistry and The California NanoSystems Institute, University of California, Los Angeles, Cali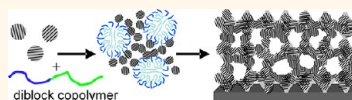fornia 90095-1569, United States, [‡]The Molecular Foundry, Lawrence Berkeley National Laboratory, Berkeley, California 94720, United States, [§]Department of Materials Science & Engineering, Cornell University, Ithaca, New York 14853, United States, and [⊥]Department of Materials Science & Engineering, University of California, Los Angeles, California 90095, United States. [‖]Present address: Laboratory of Photonics and Interfaces, École Polytechnique Fédérale de Lausanne, CH-1015 Lausanne, Switzerland.

One of the key goals of nanoscience research over the past 2 decades has been the development of methods to precisely control structure at the nanometer length scale. One route to this control that has met with significant success is amphiphilic templating of inorganic materials. In this method, soluble inorganic oligomers co-assemble with amphiphilic organic species to produce a structured inorganic/organic composite material. Thermal or chemical removal of the organic component leaves behind an inorganic material with porosity on the nanometer length scale and an architecture that is determined by co-assembly of the organic and inorganic components.[1−9] Common structure-directing agents include surfactants and block copolymers, and these have been used to prepare a broad range of mesoporous architectures from soluble inorganic building blocks, in most cases utilizing sol−gel chemistries.[10−28]

While this method provides beautiful control of nanometer scale architecture, there is much less control of the atomic scale structure in most templated nanoporous materials. Pore walls can be crystallized by thermal processing, but in many cases, the walls do not fully crystallize during template removal, resulting in a partially crystalline or amorphous pore wall.[29,30] Moreover, the lack of control of grain growth during the crystallization process can result in the destruction of the pore-solid architecture and the interconnected porosity. Creating materials with this type of nanometer scale architecture is a worthwhile goal, however, as this architecture imparts the unique combination of high

surface area, an electrically interconnected structure, and good accessibility to the surface area.

One approach to mitigate the problems associated with crystallization of the inorganic framework is to start not with sol−gel type molecular precursors but with preformed nanocrystals. Using this method, crystalline nanoporous materials can be

ABSTRACT

Block copolymer templating of inorganic materials is a robust method for the production of nanoporous materials. The method is limited, however, by the fact that the molecular inorganic precursors commonly used generally form amorphous porous materials that often cannot be crystallized with retention of porosity. To overcome this issue, here we present a general method for the production of templated mesoporous materials from preformed nanocrystal building blocks. The work takes advantage of recent synthetic advances that allow organic ligands to be stripped off of the surface of nanocrystals to produce soluble, charge-stabilized colloids. Nanocrystals then undergo evaporation-induced co-assembly with amphiphilic diblock copolymers to form a nanostructured inorganic/organic composite. Thermal degradation of the polymer template results in nanocrystal-based mesoporous materials. Here, we show that this method can be applied to nanocrystals with a broad range of compositions and sizes, and that assembly of nanocrystals can be carried out using a broad family of polymer templates. The resultant materials show disordered but homogeneous mesoporosity that can be tuned through the choice of template. The materials also show significant microporosity, formed by the agglomerated nanocrystals, and this porosity can be tuned by the nanocrystal size. We demonstrate through careful selection of the synthetic components that specifically designed nanostructured materials can be constructed. Because of the combination of open and interconnected porosity, high surface area, and compositional tunability, these materials are likely to find uses in a broad range of applications. For example, enhanced charge storage kinetics in nanoporous Mn_3O_4 is demonstrated here.

KEYWORDS: nanocrystals · evaporation-induced self-assembly · microporous · mesoporous · ligand exchange · block copolymer · templated

produced, and because thermal processing is needed only to remove the polymer template and fuse the nanocrystals into a network, and not to crystallize the inorganic phase, open, interconnected porosity is well retained. A few examples of this type of nanocrystal templating exist in the literature.[31−36] The problem is that while the literature is full of beautiful routes to soluble nanocrystals with well-defined chemical composition, size, shape, and distinctive optical, electronic, and chemical properties,[37−50] the vast majority of those nanocrystals are coated with organic surface ligands that provide solubility and prevent nanocrystal agglomeration. In order to substitute sol−gel type precursors with preformed nanocrystals in typical template-driven syntheses, the ligands must be removed from the nanocrystals while maintaining nanocrystal solubility and preventing aggregation. Most of the previous results for nanocrystal templating utilized nanocrystals with hydrolyzable surface groups that could be removed by the addition of small quantities of water to produce metastable, hydroxyl-terminated nanocrystals.[51,52] Such methods are not general, however, because in many cases removal of the surface groups leads to agglomerated nanocrystals that cannot be templated, limiting the types of nanocrystal-based nanoporous materials that can be produced.

One reason that nanocrystal templating is so important is that we have recently shown that nanocrystal-based nanoporous titania demonstrates high levels of pseudocapacitive charge storage accompanied by fast charging/discharging rates.[35] These materials were synthesized from nanocrystals that contained hydrolyzable surface ligands, as discussed above.[51,52] In that work, enhancement of electrochemical properties resulted from the unique combination of open porosity, which allowed facile electrolyte diffusion throughout the material, and the high density of electrochemically active surface redox sites, which results from the high surface area of the nanocrystal building blocks that made up the pore walls.[35] In order to be able to extend this approach to a broader array of nanocrystals, a more broadly applicable method for templating ligand-stripped nanocrystals is needed. Because of this interest in materials for electrochemical supercapacitors, the materials that we have chosen to explore in this work are either conductors or redox-active transition metal oxides. The technique should be applicable, however, to any nanocrystal system that is stable under the calcination conditions required to remove the polymer template.

Recently, there have been a few reports on methods to strip native ligands off the surface of nanocrystals to produce bare, soluble nanocrystals that can be dissolved in polar solvents.[53−55] The first example was work by Murray and co-workers, who reported a method that employed nitrosonium tetrafluoroborate (NOBF$_4$).[53] In that work, the native organic ligands are removed and replaced by some combination of protons

and dimethylformamide (DMF) to produce dispersible, cationic nanocrystals that are charge-balanced by BF$_4^-$ anions. The authors speculate that NO$^+$ reacts with trace water to form nitrous and/or fluoroboric acid which protonate basic ligands such as carboxylic acids and amines so that they desorb from the surface of nanocrystals, accompanied by phase transfer of the nanocrystals from nonpolar to polar solvents.[53] Milliron and co-workers used this method to prepare nanocomposite films containing Sn-doped In$_2$O$_3$ (ITO) nanocrystals in transition metal oxide matrices.[56] Recently, related but milder ligand-stripping methods have also been reported, so that ligands can now be removed nondestructively from a broad range of nanocrystals.[55]

In this work, we build from our previous work on templating nanocrystals into porous architectures and describe a general route to prepare hierarchical nanocrystal-based mesoporous films of various systems. The NOBF$_4$ ligand-exchange strategy is utilized to prepare dispersible nanocrystals of various systems including ITO,[56−58] manganese oxide (Mn$_3$O$_4$),[59] and manganese ferrite (MnFe$_2$O$_4$).[60] We demonstrate the generality of this approach by varying the composition and size of the nanocrystals. In addition, nanocrystals are templated with a range of diblock copolymers containing variable block compositions and molecular weights. Films are produced by various coating methods including dip-coating, spin-coating, and drop-casting. We further show that even greater material diversity is accessible through solid-state conversion reactions. For example, the MnFe$_2$O$_4$ system can be converted to a mixed manganese−iron oxide (Mn,Fe)$_2$O$_3$ with retention of the original porous architecture. Much of the significance of these results stems from the fact that nearly identical porous networks are produced from diverse nanocrystal systems with no modification of the synthetic procedure. Because this method focuses on assembly, decoupled from molecular scale reactivity and nanocrystal synthesis, procedures scale across materials systems without adjustment. Taken together, the results demonstrated in this work describe a powerful approach to templating nanocrystal systems and, therefore, a simple recipe for preparing functional nanoscale architectures from preformed nanocrystal building blocks.

RESULTS AND DISCUSSION

Preparation of Mesoporous Nanocrystal-Based Films. The synthesis of mesoporous nanocrystal-based materials is described in detail in the Materials and Methods. The key steps in the process, however, are discussed here. The overall synthetic process involves nanocrystal synthesis, ligand removal, and templating of the desired nanocrystal system. In all cases, nanocrystals were synthesized using previously reported high-temperature solution-phase syntheses that utilize organic ligands with either amine or carboxylic acid functional groups to stabilize the nanocrystal surface.[56−60]
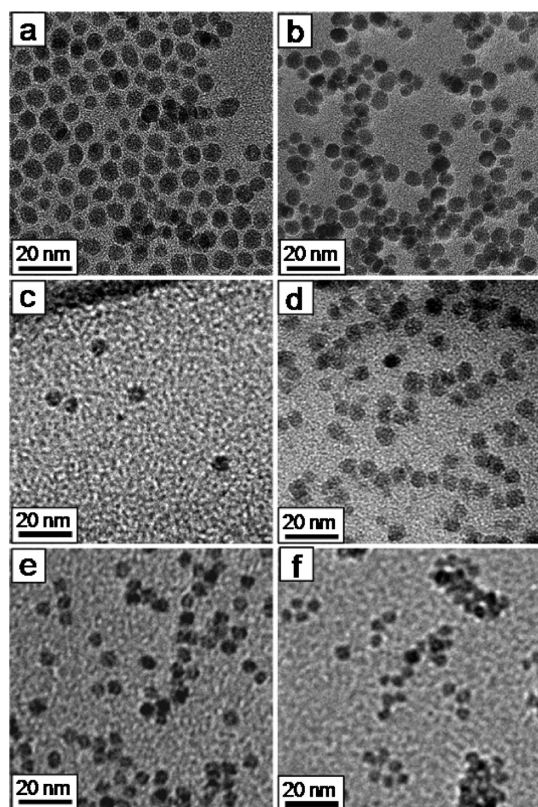
Figure 1. TEM images of ITO nanocrystals as-synthesized (a) and after the ligand-exchange process (b); $MnFe_2O_4$ nanocrystals as-synthesized (c) and after the ligand-exchange process (d); and Mn_3O_4 nanocrystals as-synthesized (e) and after the ligand-exchange process (f). In all cases, the particles do not agglomerate and maintain a uniform size and shape after the ligand removal process.

As-synthesized nanocrystals dispersed in hexane were then stripped of their surface ligands and phase transferred into polar media by treatment with $NOBF_4$ in DMF, as described above.[53] In a typical film synthesis, ethanolic dispersions of the ligand-exchanged preformed nanocrystals, with ~10% DMF (v/v), were mixed with a block copolymer template, dissolved in pure ethanol, to prepare the coating solution. Thin films were dip-coated onto clean polar substrates through an evaporation-induced self-assembly process.[61] In solution, the polymer forms micelles, and upon evaporation of the solvent, the micelles co-assemble with the preformed nanocrystals and both components self-organize into a mesostructured organic/inorganic composite. Next, the organic polymer template is thermally decomposed in air to leave behind a mesoporous inorganic architecture that exhibits three-dimensionally interconnected porosity.

Dispersible, ligand-free nanocrystal building blocks are essential to this process. Figure 1 shows the transmission electron microscopy (TEM) images of three different compositions of nanocrystals, both before and after ligand stripping with $NOBF_4$. The images show ITO (Figure 1a,b), $MnFe_2O_4$ (Figure 1c,d), and Mn_3O_4 (Figure 1e,f) nanocrystals with ligand-stripped samples

in panels b, d, and f. As can be seen in Figure 1b, $NOBF_4$-treated ITO nanocrystals are not agglomerated or fused together, suggesting they form stable dispersions.[53] A closer look at the particles after $NOBF_4$ treatment reveals a shorter interparticle distance which is consistent with removal of the native ligands.[53] In addition, the average particle size (7.3 ± 0.7 nm) does not change, suggesting no etching of the surface of the nanocrystals during the $NOBF_4$ treatment. Similar results were observed for both $MnFe_2O_4$ (Figure 1c,d) and Mn_3O_4 (Figure 1e,f) nanocrystals. There is no apparent agglomeration or change in particle size for either $MnFe_2O_4$ (4.6 ± 0.5 nm) or Mn_3O_4 (4.8 ± 0.5 nm) nanocrystals after $NOBF_4$ treatment. Taken together, the TEM data for all three systems reveal that the nanocrystals have a uniform size and shape that is not altered by the ligand removal process. These data suggest that $NOBF_4$ stripping is a viable method that can be utilized to prepare dispersions of many nanocrystal compositions for use in polymer templating.

To this end, Figure 2 shows top-view scanning electron microscope (SEM) images of mesoporous films produced from these same three nanocrystal systems including ITO (Figure 2a,b), Mn_3O_4 (Figure 2c,d), and $MnFe_2O_4$ (Figure 2e,f). For all three systems, the block copolymer template utilized was poly(ethylene-*alt*-propylene)-*block*-poly(ethylene oxide), (PEP-*b*-PEO) (polydispersity index (PDI) = 1.05), which was thermally decomposed between 350 and 450 °C in air to produce the porous materials. This class of amphiphilic block copolymers has been shown to produce well-ordered, periodic mesoporous inorganic materials.[16,35,62−72] In the synthesis, we begin with ligand-exchanged nanocrystals that are stabilized in solution by a combination of dative bonds from the DMF solvent and electrostatic repulsion from the charged nanocrystal surface. Upon evaporation of the solvent, the polar PEO block and the polar nanocrystals begin to associate, so that nanocrystals preferentially segregate to the PEO region of the composite film. Thermal treatment is then used to thermally degrade the polymer and fuse the nanocrystals together. The thermal stability of the hydrophobic polymer block ensures that the nanocrystals are well fused before full thermal decomposition of the template, resulting in a rigid inorganic porous structure.

The films in Figure 2a,b were prepared from ITO nanocrystals with a diameter of 7.3 ± 0.7 nm.[56] Figure 2a shows a low-magnification image of an ITO film where the mesopores are locally disordered, but they are macroscopically homogeneous with an average diameter of 15 ± 3 nm. The pore walls range from 1 to 3 nanocrystals across, with approximately 2 nanocrystals representing the majority of pore walls in the film. Given an average nanocrystal diameter of 7.3 ± 0.7 nm, the sum of the pore diameter and the average wall thickness is in reasonable agreement with
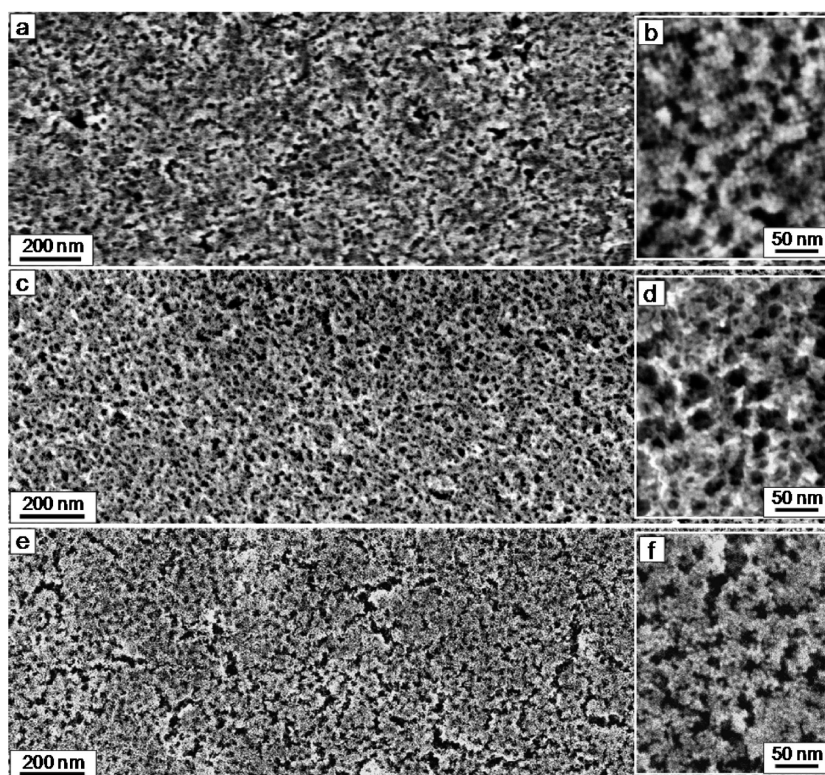
Figure 2. SEM images of various templated nanocrystal-based porous films. (a) Low-magnification and (b) high-magnification top-view SEM images of PEP-*b*-PEO templated ITO nanocrystals. (c) Low-magnification and (d) high-magnification top-view SEM images of PEP-*b*-PEO templated Mn_3O_4 nanocrystals. (e) Low-magnification and (f) high-magnification top-view SEM images of PEP-*b*-PEO templated $MnFe_2O_4$ nanocrystals.

two-dimensional small-angle X-ray scattering (see below, 2D-SAXS, Figure 6a) data where the average repeat distance was found to be 32 nm. These films are crack-free, and the pores are open at the surface. Figure 2b shows a high-magnification image where the presence of individual nanocrystals can also be seen; the voids between these nanocrystals give rise to micropores that significantly increase surface area.

Figure 2c shows a top-view low-magnification image of PEP-*b*-PEO templated Mn_3O_4 nanocrystals with an average diameter of 4.8 ± 0.5 nm.[59] A high-magnification image of Mn_3O_4 films is shown in Figure 2d. Similarly, low-magnification (Figure 2e) and high-magnification (Figure 2f) images of $MnFe_2O_4$ nanocrystal-based films with an average particle diameter of 4.6 ± 0.5 nm[60] are also shown. For these two films, just as for ITO, the mesopores are locally disordered, with an average pore diameter of 17 ± 4 nm for Mn_3O_4 films and 16 ± 2 nm for $MnFe_2O_4$ films. In the high-magnification images for both Mn_3O_4 and $MnFe_2O_4$, the presence of individual nanocrystals that give rise to micropores is again visible. In all three types of nanocrystal-based films, ITO, Mn_3O_4, and $MnFe_2O_4$, the pore walls comprise nanocrystals that fuse only at point contact and retain their generally spherical shape. Because the nanocrystals in the pore walls do not fully fuse to form a dense wall, microposity is generated.

Figure 2 thus demonstrates that our templating approach can be applied to nanocrystals with a broad range of compositions, producing films with nearly identical nanometer scale architecture. As discussed above, previous work on nanocrystal-based nanoporous solids utilized chemistries that were specific to a small class of nanocrystal systems.[35,51,52] The beauty of the $NOBF_4$ chemistry used here[53] is that it is quite general, and recent variations on the method have now extended this ligand-stripping process to even more nanocrystal types,[55] further increasing the range of materials that can be formed into porous networks.

Synthetic and Structural Tunability. To demonstrate the extent of synthetic tunability in our approach, we explored several different parameters including choice of block copolymer, coating technique, and size of the nanocrystal. In addition to the PEP-*b*-PEO polymer used to prepare the films in Figure 2, we can template films with poly(butadiene(1,2 addition))-*block*-poly-(ethylene oxide) (PB-*b*-PEO)[72] and poly(butylene oxide)-*block*-poly(ethylene oxide) (PBO-*b*-PEO). Chemically speaking, all three polymers have a PEO hydrophilic block that may vary in length and a hydrophobic block which may also vary in length. To investigate the architectural effects from each polymer template, the differences in the weight fraction and molecular weight for each block must also be considered. Here,
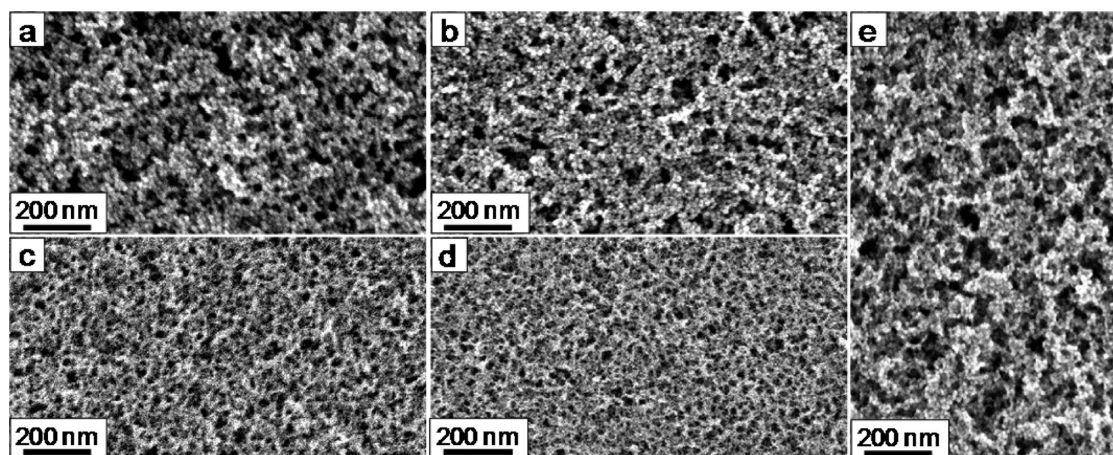
Figure 3. SEM images of templated nanocrystal-based porous films demonstrating variability of the template and coating method. Low-magnification top-view SEM images of PB-*b*-PEO templated ITO nanocrystals prepared by dip-coating (a) and spin-coating (b). Low-magnification top-view SEM images of PBO-*b*-PEO templated Mn₃O₄ nanocrystals prepared by dip-coating (c) and spin-coating (d). (e) SEM image of PEP-*b*-PEO templated ITO nanocrystals prepared by drop-casting.

the weight fraction for the PEO block, f_wPEO, in PEP-*b*-PEO is defined as f_wPEO = M_nPEO/(M_nPEO + M_nPEP), where M_nPEO and M_nPEP are the molecular weights for the individual blocks. Using this definition, the weight fractions for PEP-*b*-PEO are f_wPEP = 0.49 (M_n = 3900 g/mol) and f_wPEO = 0.51 (M_n = 4000 g/mol), for PB-*b*-PEO, they are f_wPB = 0.52 (M_n = 5500 g/mol) and f_wPEO = 0.48 (M_n = 5000 g/mol), and for PBO-*b*-PEO, they are f_wPBO = 0.57 (M_n = 6500 g/mol) and f_wPEO = 0.43 (M_n = 5000 g/mol). All polymers have similar hydrophilic/hydrophobic block ratios, but the total molecular weights and the chemical nature of the hydrophobic block vary significantly. A more detailed description of the block length, molecular weight, and weight fraction for each block in all three block copolymers can be found in the Materials and Methods.

Figure 3a,b shows top-view SEM images of PB-*b*-PEO templated ITO nanocrystals with an average diameter of 7.3 ± 0.7 nm prepared by dip-coating (Figure 3a) and spin-coating (Figure 3b). Similar to the PEP-*b*-PEO templated ITO nanocrystals in Figure 2a,b, these films demonstrate a locally disordered meso-structure with macroscopically homogeneous porosity. PB-*b*-PEO templated films have an average pore diameter of 28 ± 3 nm, and the pore walls are approximately one to three nanocrystals thick. In agreement with these values, the average distance between pores was found to be fairly large (around 36 nm) from 2D-SAXS data (Figure 6e). The variation in pore diameter and pore wall thickness for PB-*b*-PEO *versus* PEP-*b*-PEO templated ITO films can be explained by their structural difference. Our PB-*b*-PEO is a larger polymer with M_n = 10 500 g/mol, compared to PEP-*b*-PEO with M_n = 7900 g/mol. Therefore, it is expected to form larger micelles in solution, leading to larger pores. In addition, the PEO block in PB-*b*-PEO is larger than the PEO block in PEP-*b*-PEO, which should lead to thicker

pore walls since the particles co-assemble with the PEO block of the micelles to form the pore walls during synthesis.

Figure 3c,d shows top-view SEM images of Mn₃O₄ nanocrystals with an average diameter of 4−5 nm that were templated with PBO-*b*-PEO by dip-coating (Figure 3c) and spin-coating (Figure 3d). Both PB-*b*-PEO and PBO-*b*-PEO templates were thermally decomposed at 450 °C in air. Interestingly, the total molecular weight of our PBO-*b*-PEO is larger than that of our PB-*b*-PEO and PEP-*b*-PEO. However, the average pore diameter for the PBO-*b*-PEO system was found to be 13 ± 1 nm with an average pore wall thickness of 6−8 nm, which are both smaller than values determined for PB-*b*-PEO and PEP-*b*-PEO templated systems. This is corroborated with 2D-SAXS data (Figure 6f), which shows an average pore-to-pore distance of 28 nm for PBO-*b*-PEO materials, which is smaller than the average for the PB-*b*-PEO and PEP-*b*-PEO templated systems. The smaller meso-structure can be attributed to the less hydrophobic/more hydrophilic nature of the PBO block compared to PB and PEP. Some nanocrystals may associate with the nominally hydrophobic block, leading to a smaller pore. More likely, because of the increased solubility of the PBO-*b*-PEO polymer in polar solvents, the polymer may have a lower aggregation number, which could also lead to smaller-sized micelles in solution. Lower aggregation number also explains the combination of a smaller average pore diameter and a smaller pore wall thickness, which would lead to the shorter pore-to-pore distance observed in SAXS.

Figure 3e shows a top-view SEM image of ITO nanocrystals with an average diameter of 7.3 ± 0.7 nm that were templated with PEP-*b*-PEO by drop-casting. To prepare these films, nanocrystal/polymer solution was drop-cast onto a polar substrate and the solvent was allowed to evaporate in air at room temperature. The films were heated to 450 °C to thermally decompose the polymer template. The film in Figure 3e had an average thickness of 2.0 ± 0.1 μm based on

profilometry measurements. The average pore diameter was found to be 15 ± 3 nm, which is in agreement with the films in Figure 2 that were also templated with PEP-*b*-PEO. The drop-cast films show somewhat more disordered porosity, compared with dip-coated and spin-coated films. However, it is important to note that these films are at least 1 order of magnitude thicker than either dip-coated or spin-coated films, and from a macroscopic perspective, the porosity is still homogeneous.

As described above, the method used to deposit films plays a role in the final film architecture. On average, spin-coating produces the thinnest films ranging from 100 to 120 nm thick after calcination by profilometry measurements. A single dip-coating process produces films ranging from 120 to 220 nm after calcination. It was also found that multiple coatings could be used to make thicker films; for example, double-dipped films up to 400 nm could be produced. To produce thicker films, drop-casting can be used. Drop-casting is a viable method for generating films in the 1−5 μm range.

A comparison of films prepared by dip-coating (Figure 3a,c), spin-coating (Figure 3b,d), and drop-casting (Figure 3e) reveals that surface roughness increases from spin-coated < dip-coated < drop-casted films. This can be explained by differences in the drying kinetics for each coating technique. In drop-casted films, the solvent evaporates very slowly and this can lead to inhomogeneous drying, especially near the surface of the film. During dip-coating, the solvent evaporates faster than for drop-casted films but slower than spin-coated films, and these variations in evaporation rate can lead to small variations in surface roughness. On the other hand, spin-coating involves very fast evaporation of the solvent, producing films with a more homogeneous thickness. For most sol−gel-based block copolymer templated materials, spin-coating produces significantly less ordered materials because there is not enough time for hydrolysis and condensation reactions to occur during the film deposition process.[73−75] In this case, however, no chemistry occurs during film deposition, and so the pore structure in all cases is similar, indicating that all methods are viable routes to film deposition. This combination of results demonstrates the robustness of this nanocrystal templating strategy and indicates that homogeneous, nanoporous nanocrystal-based films can likely be made by any solution-phase deposition route, including industrially scalable methods such as doctor-blading or roll-to-roll deposition.

Another route to structural variation in these materials focuses on the ability to perform thermally induced solid-state conversion reactions in nanoporous materials with retention of the intrinsic nanostructure.[68,76] While many different kinds of nanocrystals can be synthesized, there are still more materials that have not yet been made as soluble nanocrystals.
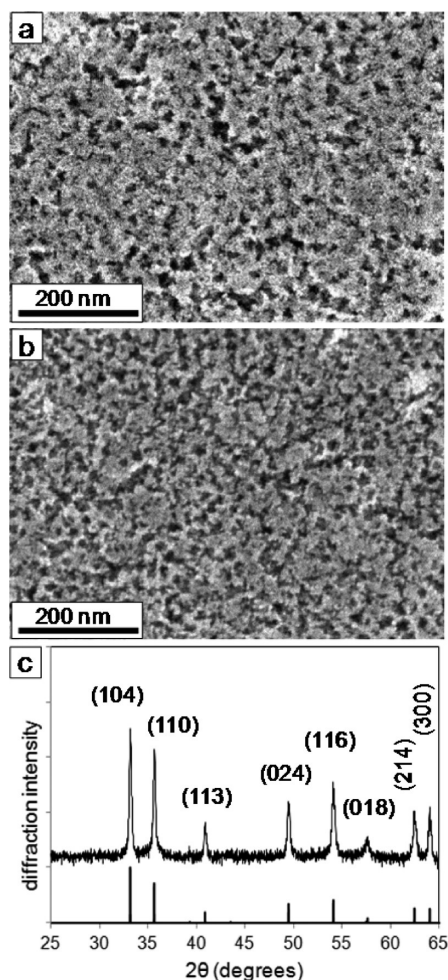
Figure 4. (a) SEM image of PEP-*b*-PEO templated MnFe$_2$O$_4$ nanocrystal-based films. (b) SEM image of MnFe$_2$O$_4$ films from (a) after thermal conversion to (Mn,Fe)$_2$O$_3$ at 400 °C, demonstrating retention of mesostrucuture. (c) WAXD data showing full conversion of MnFe$_2$O$_4$ to (Mn,Fe)$_2$O$_3$.

Solid-state transformation thus provides a route to expand the palate of accessible materials. Thermal treatments stringent enough to drive a solid−solid transformation can, however, lead to destruction of the periodicity and obstruction of the porosity from grain growth particularly at high temperatures. Here, we show one example of a transformation that can occur within our nanocrystal-based nanoporous materials with retention of nanometer scale architecture.

It is well-known that spinel-structured ferrites can be converted to materials with a hematite structure upon thermal treatment in air.[77] The data in Figure 4 demonstrate this type of solid-state conversion reaction in a PEP-*b*-PEO templated MnFe$_2$O$_4$ nanocrystal thin film. The spinel ferrite (Figure 4a) is converted to a mixed oxide (Mn,Fe)$_2$O$_3$ system (Figure 4b). The conversion of bulk spinel (cubic) MnFe$_2$O$_4$ phase to the hematite (rhombohedral) (Mn,Fe)$_2$O$_3$ phase in air at elevated temperatures (>650 °C) has been reported to occur by oxidation of the Mn^{2+} in the spinel to Mn^{3+}, resulting in a solid solution of Fe$_2$O$_3$ and Mn$_2$O$_3$ with

a hematite crystal structure.[77] The films in Figure 4a were heated to 350 °C to thermally decompose the polymer template while still retaining the ferrite phase. Interestingly, in the templated nanocrystal-based films, thermal conversion to hematite occurs at only 400 °C, which is significantly lower than the bulk conversion temperature. This result is consistent with the established fact that phase transitions in nanocrystals can occur at very different temperatures than those in the bulk systems.[78,79] More importantly, the films retain the nanoscale architecture and open porosity. Figure 4c shows WAXD data collected on converted $(Mn,Fe)_2O_3$ films. The peaks can be indexed to the hematite phase of iron oxide with a rhombohedral crystal structure (JCPDS reference card no. 08-2902) with no indication of the spinel phase suggesting complete conversion. Scherrer analysis of the peak widths gives an average grain size of ~40 nm, indicating that there is grain growth during thermal conversion. Some nanocrystals can still be seen in Figure 4b, however, suggesting an inhomogeneous distribution of grain sizes. Interestingly, the grain growth observed during the ferrite to hematite transition implies that the many nanocrystals of ferrite can convert into larger single hematite crystals with large diameters and while preserving the pore structure. The key feature to note is that the nanostructure is not destroyed, and that comparison of Figure 4a,b shows qualitatively similar porosity. This type of conversion reaction can become important when recipes for producing nanocrystals of a particular composition are not available.

Structural Characterization. While the SEM images presented in Figures 2−4 provide the most direct route to visualize these porous networks, they provide information only about a small surface region of the film, and they provide no information about the atomic scale structure of the films. To further characterize the structure of these nanocrystal-based nanoporous materials, we utilize a combination of low- and high-angle X-ray scattering, combined with ellipsometric porosimetry. Analysis of the crystal structure was carried out using wide-angle X-ray diffraction (WAXD) measurements. Figure 5a shows WAXD patterns for ITO nanocrystals as-synthesized (A), after $NOBF_4$ treatment (B), and after templating with PEP-*b*-PEO (C). In all three patterns (A−C), the evolution of the main peaks can be indexed to the cubic phase (bixbyite) of In_2O_3 with Sn doped into the lattice (JCPDS reference card no. 06-0416). Scherrer analysis of the peak widths for ITO nanocrystals as-synthesized (A) and after $NOBF_4$ treatment (B) gives in an average domain size of 7−8 nm, which is consistent with the particle size found in TEM data (Figure 1a,b). In (C), the average domain size of nanocrystals does not change after templating with PEP-*b*-PEO, which is consistent with SEM data (Figure 2a,b) that show individual nanocrystals comprising the pore walls of the films. The relative
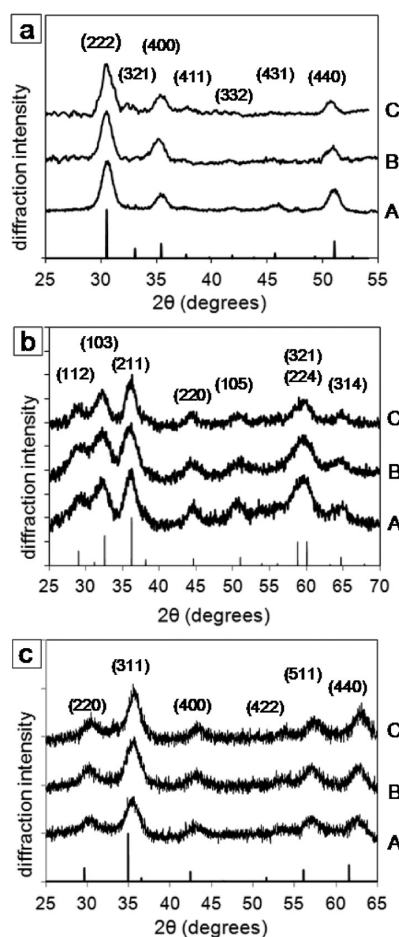

Figure 5. (a) WAXD patterns of as-synthesized ITO nanocrystals (A), ITO nanocrystals after the ligand-exchange process (B), and a templated ITO nanocrystal-based film (C). (b) WAXD patterns of as-synthesized Mn_3O_4 nanocrystals (A), Mn_3O_4 nanocrystals after the ligand-exchange process (B), and a templated Mn_3O_4 nanocrystal-based film (C). (c) WAXD patterns of as-synthesized $MnFe_2O_4$ nanocrystals (A), $MnFe_2O_4$ nanocrystals after the ligand-exchange process (B), and a templated $MnFe_2O_4$ nanocrystal-based film (C).

intensities of the peaks also suggest the nanocrystals embedded in the pore walls are randomly oriented. The fact that there is no phase transformation or grain growth during thermal decomposition of the polymer suggests the nanocrystals are thermally stable.

Similar trends were observed in both Mn_3O_4 (Figure 5b) and $MnFe_2O_4$ (Figure 5c) systems when examined by WAXD. Figure 5b shows patterns for Mn_3O_4 nanocrystals as-synthesized (A), after $NOBF_4$ treatment (B), and after templating with PEP-*b*-PEO (C). The XRD patterns for (Figure 5b (A−C)) can be assigned to the tetragonal Mn_3O_4 (hausmannite) structure (JCPDS reference card no. 80-0382). Scherrer analysis of the peak widths in all three patterns gives an average size of 4−5 nm, which is in agreement with TEM data (Figure 1e,f). Finally, for the $MnFe_2O_4$ system (Figure 5c), the main peaks in all three patterns, as-synthesized (A), after $NOBF_4$ treatment (B), and after templating with PEP-*b*-PEO (C), can be indexed to the
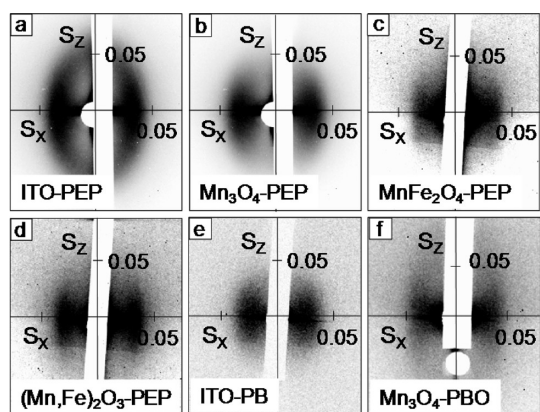
Figure 6. 2D-SAXS patterns obtained on PEP-*b*-PEO templated ITO-based films (a), Mn_3O_4-based films (b), $MnFe_2O_4$-based films (c), and $(Mn,Fe)_2O_3$-based films (d). Patterns for PB-*b*-PEO templated ITO nanocrystal-based films (e) and PBO-*b*-PEO templated Mn_3O_4 nanocrystal-based films (f). Data were collected at an angle of incidence $\beta = 1.25°$ for (a), $\beta = 2.25°$ for (b), $\beta = 0.80°$ for (c), $\beta = 0.80°$ for (d), $\beta = 0.80°$ for (e), and $\beta = 0.60°$ for (f). Scattering vector S components are given in 1/nm.

cubic phase of manganese ferrite (JCPDS reference card no. 02-8666). The average grain size for (A–C) was found to be 4–5 nm (Scherrer analysis), again confirming that the particle size is not affected by the $NOBF_4$ treatment[53] or thermal treatments, corroborating TEM (Figure 1c,d) and SEM data (Figure 4a). As in the case for ITO, analysis of the peak intensities for both Mn_3O_4 and $MnFe_2O_4$ also reveals that the pore walls are made up of nanocrystals with random orientations. Overall, the WAXD data shown here confirm that the nanocrystals for all three systems are chemically stable during $NOBF_4$ treatment[53] and thermally stable during the decomposition of the polymer. In addition, the data indicate that the nanocrystals are fully crystalline before the templating step, confirming they are in fact preformed and ready to serve as architectural building blocks.

The nanoscale architecture was further characterized by 2D-SAXS experiments, which were collected on beamline 1–4 at the Stanford Synchrotron Radiation Laboratory. Measurements were carried out in reflection mode with the incoming beam at grazing or near grazing incidence. Here we define the incident angle (*i.e.*, the angle between the X-ray beam and the plane of the substrate) as β. Higher β angles bias the diffraction against the out-of-plane scattering and are thus used for the more ordered samples to produce more even intensities around the ring. Figure 6 shows 2D-SAXS patterns collected for PEP-*b*-PEO templated films of ITO at $\beta = 1.25°$ (a), Mn_3O_4 at $\beta = 2.25°$ (b), $MnFe_2O_4$ at $\beta = 0.80°$ (c), and $(Mn,Fe)_2O_3$ $\beta = 0.80°$ (d). In the ITO-based films (a), the evolution of a diffuse ellipsoidal ring with a strong in-plane scattering maxima along the *x*-direction is observed corresponding to an average repeat distance of 32 nm. The observed pattern is characteristic of a disordered material with a homogeneous length scale. During thermal decomposition

of the polymer template, the films experience anisotropic contraction of the pores in the direction perpendicular to the plane of the substrate, which also explains the ellipsoidal shape.

The observed 2D-SAXS data for Mn_3O_4 (Figure 6b) show strong in-plane scattering maxima with an average repeat distance of 32 nm. The pattern shows a less defined ellipsoidal ring with less scattering in the *z*-direction. This type of pattern often occurs in partly disordered thin film systems. Because there are only 10–20 pore repeats through the thickness of the film, this is insufficient to produce strong constructive interference in the out-of-plane direction when disorder is included. The scattering length in the *x*- and *y*-directions is much greater, however, so constructive interference is observed even in partly disordered systems. The in-plane scattering maxima for both $MnFe_2O_4$ (Figure 6c) and $(Mn,Fe)_2O_3$ (Figure 6d) films also correspond to an average repeat distance of 32 nm.

The fact that all four types of films exhibit a similar average repeat distance is consistent with the fact that the PEP-*b*-PEO template directs the mesostructure and nanoscale architecture. Moreover, an average repeat distance of 32 nm is approximately commensurate with the sum of the average pore diameter and pore wall thickness that was estimated from SEM for all of the PEP-*b*-PEO templated nanocrystal-based materials discussed thus far. For the PB-*b*-PEO film shown in Figure 6e, a larger repeat distance (36 nm) is observed, again consistent with SEM and the large polymer size employed in the synthesis. Finally, for the PBO-*b*-PEO templated samples shown in Figure 6f, a smaller repeat distance (28 nm) is found. The reasons this polymer produces a smaller repeat distance were discussed above. While the specific repeat distance shown in Figure 6 corroborate the conclusions from SEM, the SAXS data also provide additional information. Specifically, all of the SEM images in Figures 2–4 appear to show similar levels of disorder. Examination of the SAXS data, however, shows that PEP-*b*-PEO templated films are actually somewhat more ordered at the nanometer scale than films synthesized using PB-*b*-PEO or PBO-*b*-PEO. Perhaps more importantly, the fact that scattering data can be observed for all films in 2D-SAXS regardless of the level of disorder confirms that all films show homogeneity of the structure at the nanoscale. For most applications, it is this homogeneity of pore size and wall thickness, rather than pore periodicity, that is most important.[35]

To study the effects of nanocrystal size on the porous architecture, ITO nanocrystals with an average diameter of 4.6 ± 0.4 nm (Figure 7a) and 7.3 ± 0.7 nm (Figure 7e)[56−58] were templated with PEP-*b*-PEO. For both films, the average size of the mesopores by SEM was found to be 17 ± 3 nm arising from the template. TEM images of 4.6 ± 0.4 nm ITO (Figure 7b) and 7.3 ± 0.7 nm ITO (Figure 7f) nanocrystals after $NOBF_4$ treatment show that the particles are free of agglomeration
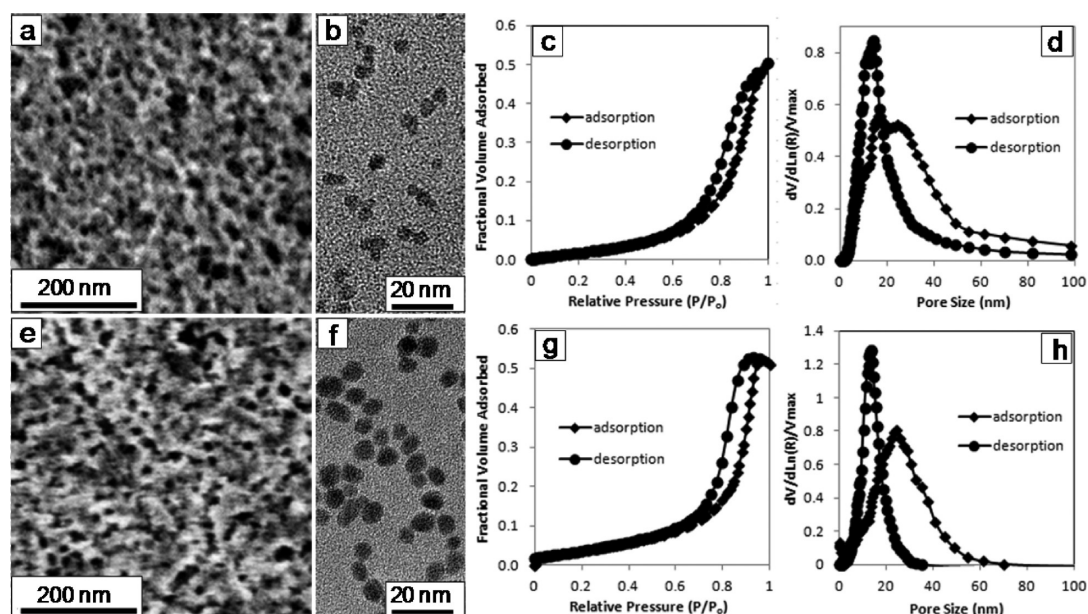
Figure 7. (a) SEM image of PEP-*b*-PEO templated ITO nanocrystals with a diameter of 4−5 nm. (b) TEM image of the NOBF$_4$-treated ITO nanocrystals. (c) Typical toluene adsorption−desorption isotherm showing characteristic mesoporous behavior for films shown in (a). (d) Pore size distribution data obtained from the isotherm in (c). (e) SEM image of 7−8 nm ITO nanocrystals templated with PEP-*b*-PEO. (f) TEM image of the NOBF$_4$-treated ITO nanocrystals. (g) Toluene adsorption−desorption isotherm showing characteristic mesoporous behavior. (h) Pore size distribution data obtained from the isotherm in (g).

with a uniform size and shape.[53] The micro- and mesoporosity were further analyzed by ellipsometric porosimetry measurements using toluene as the adsorbate.[80] Adsorption−desorption isotherms for both templated 4.6 ± 0.4 nm ITO (Figure 7c) and 7.3 ± 0.7 nm ITO (Figure 7g) nanocrystals show typical type IV behavior.[81] For this type of physisorption behavior, the presence of a hysteresis loop at higher relative pressures is representative of a mesoporous structure with interconnected porosity. The adsorption curve describes the pore size of the cages, and the desorption curve reveals the pore size of the necks. For 4.6 ± 0.4 nm ITO, a Kelvin model fit to the isotherm (Figure 7c) produces a pore diameter distribution centered at 22 nm and a neck diameter distribution centered at 12 nm, as shown in Figure 7d. The Dubinin−Radushkevich model was further fit to the isotherm at lower relative pressures to examine the micropores in these materials. Average micropore sizes for films made from 4.6 ± 0.4 nm ITO nanocrystals were 1.2 nm (cage diameter from adsorption) and 0.8 nm (neck diameter from desorption). These micropores arise from the spaces between the randomly agglomerated nanocrystals that make up the pore walls. A fit to the 7.3 ± 0.7 nm ITO isotherm (Figure 7g) gives a mesopore diameter size distribution centered on 22 nm with an average neck diameter centered on 12 nm, as shown in Figure 7h, as expected, since both films were prepared with the same polymer template. Interestingly, the micropores in this case were found to have 1.6 nm cages and 1.0 nm necks, which are larger, confirming that the size of the nanocrystals defines the micropore

structure. The isotherm for the templated 4.6 ± 0.4 nm ITO films shows a 55% toluene-accessible porous volume, while for the templated 7.3 ± 0.7 nm ITO films, it shows a 50% total pore volume.

Additional ellipsometric porosimetry measurements were carried out for PB-*b*-PEO templated 7.3 ± 0.7 nm ITO nanocrystals (Figure 8a,b) and PEP-*b*-PEO templated 4.8 ± 0.5 nm Mn$_3$O$_4$ nanocrystals (Figure 8c, d). For PB-*b*-PEO ITO, a fit to the isotherm (Figure 8a) gives a pore diameter size distribution centered on 30 nm with an average neck diameter centered on 15 nm, as shown in Figure 8b. The larger mesopores determined by porosimetry are in reasonable agreement with SEM and 2D-SAXS discussed earlier arising from the larger size of the PB-*b*-PEO template. The micropores, however, show 1.6 nm cages and 1.0 nm necks, similar to that of 7.3 ± 0.7 nm ITO templated with PEP-*b*-PEO, again confirming that the nanocrystal size dictates the microporous structure. Figure 8c shows a typical isotherm obtained for PEP-*b*-PEO templated Mn$_3$O$_4$ films. In this case, the mesopores (Figure 8d) were found to be similar to those obtained from the data in Figure 7d,h, with an average pore and neck size of 23 and 13 nm—as expected from the fact that all three samples used the same PEP-*b*-PEO template. The micropores were found to have 1.4 nm cages and 1.0 nm necks. The isotherm for the PB-*b*-PEO ITO shows a 45% toluene-accessible porous volume, while PEP-*b*-PEO Mn$_3$O$_4$ shows a 70% total pore volume. Table 1 summarizes the porosity data showing that nanocrystal-based templated films exhibit a bimodal porosity where the micropore size can be tuned by
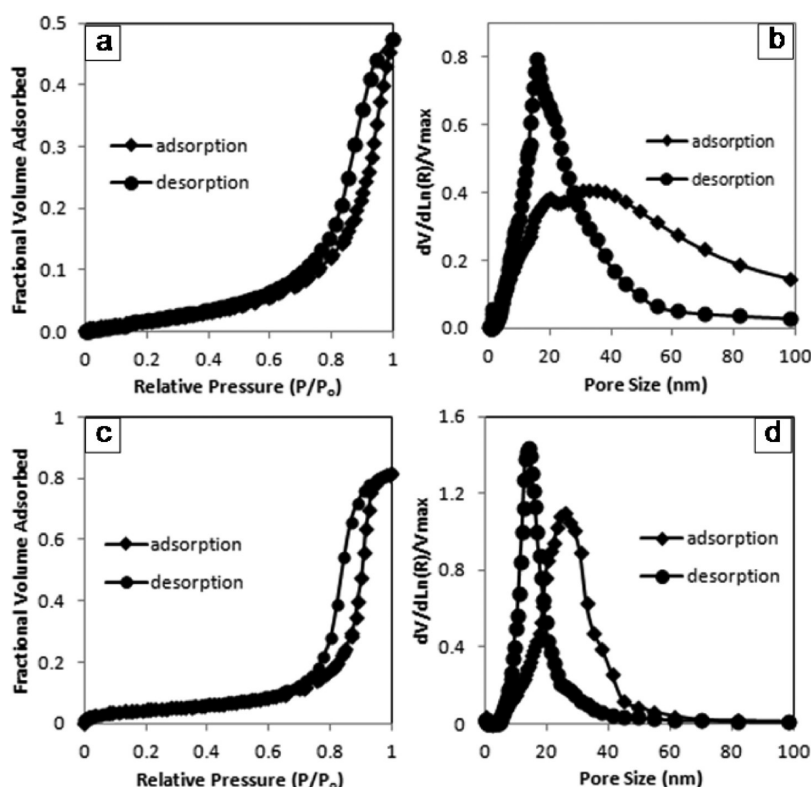
Figure 8. Toluene adsorption–desorption isotherms for PB-*b*-PEO templated ITO nanocrystals with a diameter of 7–8 nm (a) and PEP-*b*-PEO templated Mn$_3$O$_4$ nanocrystals with a diameter of 4–5 nm (c). Corresponding pore size distribution data for PB-*b*-PEO templated ITO (b) and PEP-*b*-PEO templated Mn$_3$O$_4$ (d) obtained from the isotherms.

TABLE 1. Summary of Mesopore Size Arising from the Block Copolymer Template and Micropore Size Arising from Nanocrystal Size

polymer/nanocrystal size	$M_n{}^a$ (g/mol)	f_w hydrophobic block[b]	f_w PEO block[c]	cage size (nm)[d] (mesopore from polymer) (micropore from nanocrystal)	neck size (nm)[e] (mesopore from polymer) (micropore from nanocrystal)
PEP-*b*-PEO	7900	0.49	0.51	22	12
PB-*b*-PEO	10500	0.52	0.48	30	15
PBO-*b*-PEO	11500	0.57	0.43	16	9
ITO, 4.6 nm				1.2	0.8
ITO, 7.3 nm				1.6	1.0
Mn$_3$O$_4$, 4.8 nm				1.4	1.0

[a] Total molecular weight of the block copolymer template. [b] Weight fraction for the hydrophobic block. [c] Weight fraction for the PEO block. [d] Average cage size for mesopores arising from the template or micropores arising from the nanocrystal size. [e] Average neck size for mesopores arising from the template or micropores arising from the nanocrystal size.

changing the size of the preformed nanocrystals and the mesopore size can be tuned by changing the size and chemical nature of the template. Overall, the pore analyses found here corroborate the observations from SEM, TEM, WAXD, and 2D-SAXS described earlier in all systems studied.

To demonstrate the advantage of our high surface area mesoporous architecture materials, we examined the electrochemical properties of a templated Mn$_3$O$_4$ nanocrystal-based mesoporous film and compared it to an untemplated film, cast from the same ligand-free nanocrystals. Figure 9 shows a comparison of charging times calculated from cyclic voltammetric data at

various sweep rates for a PEP-*b*-PEO templated Mn$_3$O$_4$ nanocrystal-based mesoporous film (squares) and an untemplated Mn$_3$O$_4$ nanocrystal film (circles) cycled in a non-aqueous electrolyte. The data show significant differences in charging behavior for the two films. The most obvious trend is the total capacity; after 500 s, the total charge stored in the templated film is about 300 C/g, twice the amount of charge compared to the untemplated film (150 C/g). Perhaps more important is the time-dependent trends. After 1200 s, the templated film is fully charged while the capacity in the untemplated films is still increasing at 2500 s. The templated film stores more charge than the
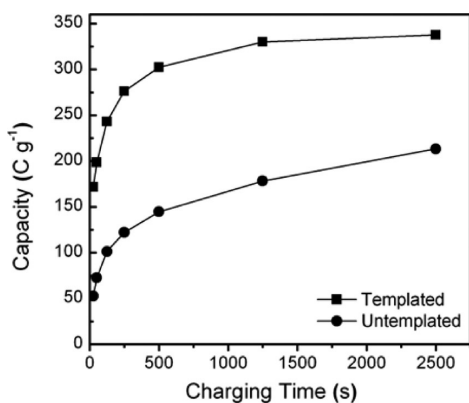
Figure 9. Comparison of capacity at various charging times calculated from cyclic voltammetric data at various sweep rates for a PEP-*b*-PEO templated Mn_3O_4 nanocrystal-based mesoporous film (squares) and an untemplated Mn_3O_4 nanocrystal film (circles).

untemplated film because the pore structure maximizes surface area and thus accessible redox sites. Moreover, comparison of the templated film to the untemplated film shows that the open and interconnected porosity enhances charge storage kinetics by facilitating ion/electrolyte diffusion to the redox sites.

CONCLUSIONS

In this work, we describe a general route for assembling preformed nanocrystals into hierarchical mesoporous architectures. By tailoring the nanocrystal composition and size along with the block copolymer template type and size, the methodology presented here can offer a high degree of synthetic and structural control over the final architecture of the material. In addition, the ability to perform solid-state conversion reactions while retaining the structure/porosity was also demonstrated. The $NOBF_4$ ligand-exchange method used here resulted in soluble nanocrystals without any particle etching or growth, or change in crystal structure, suggesting this general method may be extended to a wider range of functional nanocrystals. As a demonstration of the utility of these materials, we show enhanced charge storage kinetics for porous Mn_3O_4 films. Many of the polymer templates used here are commercially available, indicating that this is a generally accessible route to the production of nanocrystal-based nanoporous materials. Moreover, while the materials presented here showed homogeneous, but disordered porosity, recent advances using custom synthesized polymers indicate that highly ordered materials can also be produced from ligand-stripped nanocrystals.[82]

Taken together, this work provides a general strategy for harnessing the incredible synthetic diversity of nanocrystal-based materials and using it for the production of nanoporous materials. This general route should be applicable to many nanocrystal systems for a wide range of applications.

MATERIALS AND METHODS

Materials. The following chemicals were purchased and used as received: oleylamine (90% Aldrich), oleic acid (90%, Aldrich), stearic acid (95%, Aldrich), xylene (98%, Aldrich), manganese(II) acetate (98%, Aldrich), indium acetylacetonate (99.99+%, Aldrich), tin bis(acetylacetonate) dichloride (98%, Aldrich), manganese(II) acetylacetonate (Aldrich), iron(III) acetylacetonate (97% Aldrich), 1,2-hexadecanediol (90%, Aldrich), benzyl ether (98%, Aldrich), and nitrosonium tetrafluoroborate (95%, Aldrich). Poly(butadiene-(1,2 addition))-*b*-poly(ethylene oxide), with a mass ratio of PB(5500)-*b*-PEO(5000), a block ratio of PB_{102}-*b*-PEO_{114}, and with a polydispersity index (PDI) = 1.05, was purchased from Polymer Source, Inc. Poly(butylene oxide)-*b*-poly(ethylene oxide), with a mass ratio of PBO(5000)-*b*-PEO(6500), a block ratio PBO_{90}-*b*-PEO_{114}, and with a PDI = 1.09, was purchased from Advanced Polymer Materials Inc. Poly((ethylene-*alt*-propylene)-*block*-poly-(ethylene oxide), with a mass ratio of PEP(3900)-*b*-PEO(4000), a block ratio of PEP_{56}-*b*-PEO_{91}, and with a PDI = 1.05, was synthesized using reported methods.[83,84] Briefly, polyisoprene was grown by anionic polymerization, terminated with an —OH group, and then hydrogenated over Pd/C. The resulting PEP—OH was subsequently extended by anionic polymerization of ethylene oxide.

Synthesis and Ligand Exchange of Nanocrystals. Previously reported procedures were followed to synthesize 7–8 and 4–5 nm ITO nanocrystals,[56–58] 4–5 nm $MnFe_2O_4$ nanocrystals,[60] and 4–5 nm Mn_3O_4 nanocrystals,[59] all of which were stabilized by either oleylamine or oleic acid ligands. All as-synthesized nanocrystals were purified and dispersed in hexane (10–15 mg/mL). To carry out the ligand-exchange process, as-synthesized nanocrystals were treated with $NOBF_4$ according to a recently reported procedure.[53] In a typical ligand-exchange reaction, 5 mL of nanocrystal dispersion in hexane was combined with 5 mL of $NOBF_4$ solution in *N,N*-dimethylformamide (DMF) (10 mg/mL) with stirring (5 min), or until the nanocrystals were transferred to the DMF phase. The nanocrystals were precipitated with toluene then centrifuged, followed by multiple washings with DMF/toluene. The ligand-stripped nanocrystals were dispersed in DMF/ethanol (1:10 v/v) to give a final concentration of 15–20 mg/mL.

Synthesis of Mesoporous Nanocrystal-Based Films. In a typical synthesis, 40 mg of the desired diblock copolymer was dissolved in 0.5 mL of ethanol with gentle heating. To this solution was added 3 mL of the desired nanocrystals in DMF/ethanol (20 mg/mL). From this mixture, thin films were produced by dip-coating onto polar substrates at a constant withdrawal rate of 1–10 mm/s with a constant 30% relative humidity. Thin films were also prepared by spin-coating onto polar substrates at 1000 to 2000 rpm for 60 s. Finally, thick films could be produced by drop-casting onto polar substrates. In most cases, some optimization of the exact concentration of diblock copolymer and nanocrystal was required for mesostructure optimization. The films were dried using a 3 h ramp up to 175 °C, followed by a 3 h soak. Thermal decomposition of the template was done after the drying step using a 6 h ramp from 175 to 450 °C for ITO and Mn_3O_4 films and to 350 °C for $MnFe_2O_4$ films, followed by a 3 h soak.

Methods. Transmission electron microscopy (TEM) images were obtained using an FEI/PHILIPS CM120 electron microscope operating at 120 kV, as well as a JEOL-2100 electron microscope operating at 200 kV. Scanning electron microscopy (SEM) images were obtained using a JEOL model 6700F electron microscope with beam energy of 5 kV and with a Zeiss Gemini Ultra-55 analytical electron microscope with beam energy of 5 kV. Conventional wide-angle X-ray diffraction (WAXD)

measurements were carried out on a Bruker D8-GADDS diffractometer with Cu Kα radiation and on a Panalytical XPert PRO MPD diffractometer, again with Cu Kα radiation. Two-dimensional small-angle X-ray scattering (2D-SAXS) data were collected at the Stanford Synchrotron Radiation Laboratory using beamline 1-4 using the Rayonix165 large-angle CCD detector. All measurements were performed in reflection geometry. Ellipsometric porosimetry was performed on a PS-1000 instrument from Semilab using toluene as the adsorbate. A UV−visible CCD detector adapted to a grating spectrograph analyzes the signal reflected by the sample. The light source is a 75 W Hamamatsu xenon lamp, and measurements were performed on the spectral range from 1.24 to 4.5 eV. Data analysis was performed using the associated WinElli II software using the assumption of slit-like mesopores. If the mesopores are more cylindrical, actual mesopore sizes could be slightly larger than the values reported here. Electrochemical measurements were carried out in a three-electrode cell using a PAR EG&G 273A potentiostat in an argon-filled glovebox, with oxygen and water levels <1 ppm. The working electrode consisted of ITO glass upon which Mn_3O_4 films were deposited. The electrolyte solution used was 1.0 M $LiClO_4$ in propylene carbonate (PC), and lithium metal foils were used as the counter and reference electrodes. Cyclic voltammetry was performed using cutoff voltages at 4 and 1.5 V vs Li/Li$^+$.

Conflict of Interest: The authors declare no competing financial interest.

REFERENCES AND NOTES

1. Kresge, C. T.; Leonowicz, M. E.; Roth, W. J.; Vartuli, J. C.; Beck, J. S. Ordered Mesoporous Molecular Sieves Synthesized by a Liquid-Crystal Template Mechanism. *Nature* **1992**, *359*, 710–712.

2. Beck, J. S.; Vartuli, J. C.; Roth, W. J.; Leonowicz, M. E.; Kresge, C. T.; Schmitt, K. D.; Chu, C. T.-W.; Olson, D. H.; Sheppard, E. W.; McCullen, S. B.; et al. A New Family of Mesoporous Molecular Sieves Prepared with Liquid Crystal Templates. *J. Am. Chem. Soc.* **1992**, *114*, 10834–10843.

3. Zhao, D.; Feng, J.; Huo, Q.; Melosh, N.; Fredrickson, G. H.; Chmelka, B. F.; Stucky, G. D. Triblock Copolymer Syntheses of Mesoporous Silica with Periodic 50 to 300 Angstrom Pores. *Science* **1998**, *279*, 548–552.

4. Yanagisawa, T.; Shimizu, T.; Kuroda, K.; Kato, C. The Preparation of Alkyltrimethylammonium-Kanemite Complexes and Their Conversion to Microporous Materials. *Bull. Chem. Soc. Jpn.* **1990**, *63*, 988–992.

5. Inagaki, S.; Fukushima, Y.; Kuroda, K. Synthesis of Highly Ordered Mesoporous Materials from a Layered Polysilicate. *J. Chem. Soc., Chem. Commun.* **1993**, 680–682.

6. Ogawa, M. Formation of Novel Oriented Transparent Films of Layered Silica-Surfactant Nanocomposites. *J. Am. Chem. Soc.* **1994**, *116*, 7941–7942.

7. Antonelli, D. M.; Ying, J. Y. Synthesis of Hexagonally Packed Mesoporous TiO_2 by a Modified Sol−Gel Method. *Angew. Chem., Int. Ed. Engl.* **1995**, *34*, 2014–2017.

8. Yang, H.; Kuperman, A.; Coombs, N.; Mamiche-Afara, S.; Ozin, G. A. Synthesis of Oriented Films of Mesoporous Silica on Mica. *Nature* **1996**, *379*, 703–705.

9. Monnier, A.; Schuth, F.; Huo, Q.; Kumar, D.; Margolese, D.; Maxwell, R. S.; Stucky, G. D.; Krishnamurty, M.; Petroff, P.; Firouzi, A.; et al. Cooperative Formation of Inorganic−Organic Interfaces in the Synthesis of Silicate Mesostructures. *Science* **1993**, *261*, 1299–1303.

10. Brezesinski, K.; Haetge, J.; Wang, J.; Mascotto, S.; Reitz, C.; Rein, A.; Tolbert, S. H.; Perlich, J.; Dunn, B.; Brezesinski, T. Ordered Mesoporous α-Fe_2O_3 (Hematite) Thin-Film Electrodes for Application in High Rate Rechargeable Lithium Batteries. *Small* **2011**, *7*, 407–414.

11. Sun, D.; Riley, A. E.; Cadby, A. J.; Richman, E. K.; Korlann, S. D.; Tolbert, S. H. Hexagonal Nanoporous Germanium through Surfactant-Driven Self-Assembly of Zintl Clusters. *Nature* **2006**, *441*, 1126–1130.

12. Stefik, M.; Mahajan, S.; Sai, H.; Epps, T. H.; Bates, F. S.; Gruner, S. M.; DiSalvo, F. J.; Wiesner, U. Ordered Three- and Five-Ply Nanocomposites from ABC Block Terpolymer Microphase Separation with Niobia and Aluminosilicate Sols. *Chem. Mater.* **2009**, *21*, 5466–5473.

13. Deng, Y.; Yu, T.; Wan, Y.; Shi, Y.; Meng, Y.; Gu, D.; Zhang, L.; Huang, Y.; Liu, C.; Wu, X.; et al. Ordered Mesoporous Silicas and Carbons with Large Accessible Pores Templated from Amphiphilic Diblock Copolymer Poly-(ethylene oxide)-*b*-Polystyrene. *J. Am. Chem. Soc.* **2007**, *129*, 1690–1697.

14. Cheng, Y. J.; Gutmann, J. S. Morphology Phase Diagram of Ultrathin Anatase TiO_2 Films Templated by a Single PS-*b*-PEO Block Copolymer. *J. Am. Chem. Soc.* **2006**, *128*, 4658–4674.

15. Mamak, M.; Coombs, N.; Ozin, G. Mesoporous Yttria-Zirconia and Metal-Yttria-Zirconia Solid Solutions for Fuel Cells. *Adv. Mater.* **2000**, *12*, 198–202.

16. Warren, S. C.; Perkins, M. R.; Adams, A. M.; Kamperman, M.; Burns, A. A.; Arora, H.; Herz, E.; Suteewong, T.; Sai, H.; Li, Z.; et al. A Silica Sol−Gel Design Strategy for Nanostructured Metallic Materials. *Nat. Mater.* **2012**, *11*, 460–467.

17. Stefik, M.; Lee, J.; Wiesner, U. Nanostructured Carbon-Crystalline Titania Composites from Microphase Separation of Poly(ethylene oxide-*b*-acrylonitrile) and Titania Sols. *Chem. Commun.* **2009**, 2532–2534.

18. Tian, B. Z.; Liu, X. Y.; Tu, B.; Yu, C. Z.; Fan, J.; Wang, L. M.; Xie, S. H.; Stucky, G. D.; Zhao, D. Self-Adjusted Synthesis of Ordered Stable Mesoporous Minerals by Acid−Base Pairs. *Nat. Mater.* **2003**, *2*, 159–163.

19. Finnemore, A. S.; Scherer, M. R. J.; Langford, R.; Mahajan, S.; Ludwigs, S.; Meldrum, F. C.; Steiner, U. Nanostructured Calcite Single Crystals with Gyroid Morphologies. *Adv. Mater.* **2009**, *21*, 3928–3932.

20. Brezesinski, T.; Wang, J.; Senter, R.; Brezesinski, K.; Dunn, B.; Tolbert, S. H. On the Correlation between Mechanical Flexibility, Nanoscale Structure, and Charge Storage in Periodic Mesoporous CeO_2 Thin Films. *ACS Nano* **2010**, *4*, 967–977.

21. Yang, P.; Deng, T.; Zhao, D.; Feng, P.; Pine, D.; Chmelka, B.; Whitesides, G.; Stucky, G. D. Hierarchically Ordered Oxides. *Science* **1998**, *282*, 2244–2246.

22. Freer, E. M.; Krupp, L. E.; Hinsberg, W. D.; Rice, P. M.; Hedrick, J. L.; Cha, J. N.; Miller, R. D.; Kim, H. C. Oriented Mesoporous Organosilicate Thin Films. *Nano Lett.* **2005**, *5*, 2014–2018.

23. Brezesinski, T.; Groenewolt, M.; Gibaud, A.; Pinna, N.; Antonietti, M.; Smarsly, B. Evaporation-Induced Self-Assembly (EISA) at Its Limit: Ultrathin, Crystalline Patterns by Templating of Micellar Monolayers. *Adv. Mater.* **2006**, *18*, 2260–2263.

24. Grosso, D.; Boissière, C.; Smarsly, B.; Brezesinski, T.; Pinna, N.; Albouy, P. A.; Amenitsch, H.; Antonietti, M.; Sanchez, C. Periodically Ordered Nanoscale Islands and Mesoporous Films Composed of Nanocrystalline Multimetallic Oxides. *Nat. Mater.* **2004**, *3*, 787–792.

25. Kuemmel, M.; Grosso, D.; Boissière, C.; Smarsly, B.; Brezesinski, T.; Albouy, P. A.; Amenitsch, H.; Sanchez, C. Thermally Stable Nanocrystalline γ-Alumina Layers with

Highly Ordered 3D Mesoporosity. *Angew. Chem., Int. Ed.* **2005**, *11*, 4665–4668.

26. Docampo, P.; Guldin, S.; Stefik, M.; Tiwana, P.; Orilall, M. C.; Huttner, S.; Sai, H.; Wiesner, U.; Steiner, U.; Snaith, H. J. Control of Solid-State Dye-Sensitized Solar Cell Performance by Block-Copolymer-Directed TiO₂ Synthesis. *Adv. Funct. Mater.* **2010**, *20*, 1787–1796.

27. Zhao, D.; Huo, Q.; Feng, J.; Chmelka, B. F.; Stucky, G. D. Nonionic Triblock and Star Diblock Copolymer and Oligomeric Surfactant Syntheses of Highly Ordered, Hydrothermally Stable, Mesoporous Silica Structures. *J. Am. Chem. Soc.* **1998**, *120*, 6024–6036.

28. Kondo, J. N.; Domen, K. Crystallization of Mesoporous Metal Oxides. *Chem. Mater.* **2008**, *20*, 835–847.

29. Crepaldi, E. L.; Soler-Illia, G. J. A. A.; Grosso, D.; Sanchez, C. Nanocrystallised Titania and Zirconia Mesoporous Thin Films Exhibiting Enhanced Thermal Stability. *New J. Chem.* **2003**, *27*, 9–13.

30. Crepaldi, E. L.; Soler-Illia, G. J. A. A.; Grosso, D.; Cagnol, F.; Ribot, F.; Sanchez, C. Controlled Formation of Highly Organized Mesoporous Titania Thin Films: From Mesostructured Hybrids to Mesoporous Nano-anatase TiO₂. *J. Am. Chem. Soc.* **2003**, *125*, 9770–9786.

31. Warren, S. C.; Messina, L. C.; Slaughter, L. S.; Kamperman, M.; Zhou, Q.; Gruner, S. M.; DiSalvo, F. J.; Wiesner, U. Ordered Mesoporous Materials from Metal Nanoparticle-Block Copolymer Self-Assembly. *Science* **2008**, *320*, 1748–1752.

32. Corma, A.; Atienzar, P.; Garcia, H.; Chane-Ching, J. Y. Hierarchically Mesostructured Doped CeO₂ with Potential for Solar-Cell Use. *Nat. Mater.* **2004**, *3*, 394–397.

33. Deshpande, A. S.; Pinna, N.; Smarsly, B.; Antonietti, M.; Niederberger, M. Controlled Assembly of Preformed Ceria Nanocrystals into Highly Ordered 3D Nanostructures. *Small* **2005**, *1*, 313–316.

34. Ba, J.; Polleux, J.; Antonietti, M.; Niederberger, M. Nonaqueous Synthesis of Tin Oxide Nanocrystals and Their Assembly into Ordered Porous Mesostructures. *Adv. Mater.* **2005**, *17*, 2509–2512.

35. Brezesinski, T.; Wang, J.; Polleux, J.; Dunn, B.; Tolbert, S. H. Templated Nanocrystal-Based Porous TiO₂ Films for Next-Generation Electrochemical Capacitors. *J. Am. Chem. Soc.* **2009**, *131*, 1802–1809.

36. Szeifert, J. M.; Feckl, J. M.; Fattakhova-Rohlfing, D.; Liu, Y.; Kalousek, V.; Rathousky, J.; Bein, T. Ultrasmall Titania Nanocrystals and Their Direct Assembly into Mesoporous Structures Showing Fast Lithium Insertion. *J. Am. Chem. Soc.* **2010**, *132*, 12605–12611.

37. Sun, S.; Murray, C. B. Synthesis of Monodisperse Cobalt Nanocrystals and Their Assembly into Magnetic Superlattices. *J. Appl. Phys.* **1999**, *85*, 4325–4330.

38. Boyer, J.-C.; Vetrone, F.; Cuccia, L. A.; Capobianco, J. A. Synthesis of Colloidal Upconverting NaYF₄ Nanocrystals Doped with Er³⁺, Yb³⁺ and Tm³⁺, Yb³⁺ *via* Thermal Decomposition of Lanthanide Trifluoroacetate Precursors. *J. Am. Chem. Soc.* **2006**, *128*, 7444–7445.

39. Shevchenko, E. V.; Talapin, D. V.; Rogach, A. L.; Kornowski, A.; Haase, M.; Weller, H. Colloidal Synthesis and Self-Assembly of CoPt₃ Nanocrystals. *J. Am. Chem. Soc.* **2002**, *124*, 11480–11485.

40. Manna, L.; Milliron, D. J.; Meisel, A.; Scher, E. C.; Alivisatos, A. P. Controlled Growth of Tetrapod-Branched Inorganic Nanocrystals. *Nat. Mater.* **2003**, *2*, 382–385.

41. Hines, M. A.; Guyot-Sionnest, P. Synthesis and Characterization of Strongly Luminescing ZnS-Capped CdSe Nanocrystals. *J. Phys. Chem.* **1996**, *100*, 468–471.

42. Peng, X.; Schlamp, M. C.; Kadavanich, A. V.; Alivisatos, A. P. Epitaxial Growth of Highly Luminescent CdSe/CdS Core/Shell Nanocrystals with Photostability and Electronic Accessibility. *J. Am. Chem. Soc.* **1997**, *119*, 7019–7029.

43. Xia, Y.; Xiong, Y. J.; Lim, B.; Skrabalak, S. E. Shape-Controlled Synthesis of Metal Nanocrystals: Simple Chemistry Meets Complex Physics? *Angew. Chem., Int. Ed.* **2009**, *48*, 60–103.

44. Yu, W. W.; Falkner, J. C.; Shih, B. S.; Colvin, V. L. Preparation and Characterization of Monodisperse PbSe Semiconductor Nanocrystals in a Noncoordinating Solvent. *Chem. Mater.* **2004**, *16*, 3318–3322.

45. Murray, C. B.; Norris, D. J.; Bawendi, M. G. Synthesis and Characterization of Nearly Monodisperse CdE (E = Sulfur, Selenium, Tellurium) Semiconductor Nanocrystallites. *J. Am. Chem. Soc.* **1993**, *115*, 8706–8715.

46. Chen, O.; Chen, X.; Yang, Y.; Lynch, J.; Wu, H.; Zhuang, J.; Cao, Y. C. Synthesis of Metal-Selenide Nanocrystals Using Selenium Dioxide as the Selenium Precursor. *Angew. Chem., Int. Ed.* **2008**, *47*, 8638–8641.

47. Sun, Y.; Xia, Y. Shape-Controlled Synthesis of Gold and Silver Nanoparticles. *Science* **2002**, *298*, 2176–2179.

48. Peng, X.; Manna, L.; Yang, W.; Wickham, J.; Scher, E.; Kadavanich, A.; Alivisatos, A. P. Shape Control of CdSe Nanocrystals. *Nature* **2000**, *404*, 59–61.

49. Gaponik, N.; Talapin, D. V.; Rogach, A. L.; Hoppe, K.; Shevchenko, E. V.; Kornowski, A.; Eychmuller, A.; Weller, H. Thiol-Capping of CdTe Nanocrystals: An Alternative to Organometallic Synthetic Routes. *J. Phys. Chem. B* **2002**, *106*, 7177–7185.

50. Talapin, D. V.; Yu, H.; Shevchenko, E. V.; Lobo, A.; Murray, C. B. Synthesis of Colloidal PbSe/PbS Core-Shell Nanowires and PbS/Au Nanowire–Nanocrystal Heterostructures. *J. Phys. Chem. C* **2007**, *111*, 14049–14054.

51. Niederberger, M.; Bartl, M. H.; Stucky, G. D. Benzyl Alcohol and Titanium Tetrachloride—A Versatile Reaction System for the Nonaqueous and Low-Temperature Preparation of Crystalline and Luminescent Titania Nanoparticles. *Chem. Mater.* **2002**, *14*, 4364–4370.

52. Niederberger, M.; Garnweitner, G.; Krumeich, F.; Nesper, R.; Colfen, H.; Antonietti, M. Tailoring the Surface and Solubility Properties of Nanocrystalline Titania by a Nonaqueous *In Situ* Functionalization Process. *Chem. Mater.* **2004**, *16*, 1202–1208.

53. Dong, A.; Ye, X.; Chen, J.; Kang, Y.; Gordon, T.; Kikkawa, J. M.; Murray, C. B. A Generalized Ligand-Exchange Strategy Enabling Sequential Surface Functionalization of Colloidal Nanocrystals. *J. Am. Chem. Soc.* **2011**, *133*, 998–1006.

54. Nag, A.; Kovalenko, M. V.; Lee, J.-S.; Liu, W.; Spokoyny, B.; Talapin, D. V. Metal-Free Inorganic Ligands for Colloidal Nanocrystals: S²⁻, HS⁻, Se²⁻, HSe⁻, Te²⁻, HTe⁻, TeS₃²⁻, OH⁻, and NH²⁻ as Surface Ligands. *J. Am. Chem. Soc.* **2011**, *133*, 10612–10620.

55. Rosen, E. L.; Buonsanti, R.; Llordes, A.; Sawvel, A. M.; Milliron, D. J.; Helms, B. A. Exceptionally Mild Reactive Stripping of Native Ligands from Nanocrystal Surfaces by Using Meerwein's Salt. *Angew. Chem., Int. Ed.* **2012**, *51*, 684–689.

56. Llordes, A.; Hammack, A. T.; Buonsanti, R.; Tangirala, R.; Aloni, S.; Helms, B. A.; Milliron, D. J. Polyoxometalates and Colloidal Nanocrystals as Building Blocks for Metal Oxide Nanocomposite Films. *J. Mater. Chem.* **2011**, *21*, 11631–11638.

57. Choi, S. -I.; Nam, K. M.; Park, B. K.; Seo, W. S.; Park, J. T. Preparation and Optical Properties of Colloidal, Monodisperse, and Highly Crystalline ITO Nanoparticles. *Chem. Mater.* **2008**, *20*, 2609–2611.

58. Giltsrap, R. A.; Capozzi, C. J.; Carson, C. G.; Gerhardt, R. A.; Summers, C. J. Synthesis of a Nonagglomerated Indium Tin Oxide Nanoparticle Dispersion. *Adv. Mater.* **2008**, *20*, 4163–4166.

59. Yu, T.; Moon, J.; Park, J.; Park, Y. I.; Na, H. B.; Kim, B. H.; Song, I. C.; Moon, W. K.; Hyeon, T. Various-Shaped Uniform Mn₃O₄ Nanocrystals Synthesized at Low Temperature in Air Atmosphere. *Chem. Mater.* **2009**, *21*, 2272–2279.

60. Masala, O.; Seshadri, R. Magnetic Properties of Capped, Soluble MnFe₂O₄ Nanoparticles. *Chem. Phys. Lett.* **2005**, *402*, 160–164.

61. Lu, Y.; Ganguli, R.; Drewien, C. A.; Anderson, M. T.; Brinker, C. J.; Gong, W.; Guo, Y.; Soyez, H.; Dunn, B.; Huang, M. H.; *et al.* Continuous Formation of Supported Cubic and Hexagonal Mesoporous Films by Sol−Gel Dip-Coating. *Nature* **1997**, *389*, 364–368.

62. Garcia, B. C.; Kamperman, M.; Ulrich, R.; Jain, A.; Gruner, S. M.; Wiesner, U. Morphology Diagram of a Diblock Copolymer−Aluminosilicate Nanoparticle System. *Chem. Mater.* **2009**, *21*, 5397–5405.

63. Brezesinski, T.; Wang, J.; Tolbert, S. H.; Dunn, B. Ordered Mesoporous α-MoO$_3$ with Iso-Oriented Nanocrystalline Walls for Thin-Film Pseudocapacitors. *Nat. Mater.* **2010**, *9*, 146–151.

64. Haetge, J.; Hartmann, P.; Brezesinski, K.; Janek, J.; Brezesinski, T. Ordered Large-Pore Mesoporous Li$_4$Ti$_5$O$_{12}$ Spinel Thin Film Electrodes with Nanocrystalline Framework for High Rate Rechargeable Lithium Batteries: Relationships among Charge Storage, Electrical Conductivity, and Nanoscale Structure. *Chem. Mater.* **2011**, *23*, 4384–4393.

65. Sallard, S.; Brezesinski, T.; Smarsly, B. M. Electrochromic Stability of WO$_3$ Thin Films with Nanometer-Scale Periodicity and Varying Degrees of Crystallinity. *J. Phys. Chem. C* **2007**, *111*, 7200–7206.

66. Quickel, T. E.; Le, V. H.; Brezesinski, T.; Tolbert, S. H. On the Correlation between Nanoscale Structure and Magnetic Properties in Ordered Mesoporous Cobalt Ferrite (CoFe$_2$O$_4$) Thin Films. *Nano Lett.* **2010**, *10*, 2982–2988.

67. Haetge, J.; Suchomski, C.; Brezesinski, T. Ordered Mesoporous MFe$_2$O$_4$ (M = Co, Cu, Mg, Ni, Zn) Thin Films with Nanocrystalline Walls, Uniform 16 nm Diameter Pores and High Thermal Stability: Template-Directed Synthesis and Characterization of Redox Active Trevorite. *Inorg. Chem.* **2010**, *49*, 11619–11626.

68. Richman, E. K.; Kang, C. B.; Brezesinski, T.; Tolbert, S. H. Ordered Mesoporous Silicon through Magnesium Reduction of Polymer Templated Silica Thin Films. *Nano Lett.* **2008**, *8*, 3075–3079.

69. Suchomski, C.; Reitz, C.; Brezesinski, K.; Tavares de Sousa, C.; Rohnke, M.; Iimura, K.; Esteves de Araujo, J. P.; Brezesinski, T. Structural, Optical, and Magnetic Properties of Highly Ordered Mesoporous MCr$_2$O$_4$ and MCr$_{2−x}$Fe$_x$O$_4$ (M = Co, Zn) Spinel Thin Films with Uniform 15 nm Diameter Pores and Tunable Nanocrystalline Domain Sizes. *Chem. Mater.* **2012**, *24*, 155–165.

70. Brezesinski, K.; Wang, J.; Haetge, J.; Reitz, C.; Steinmueller, S. O.; Tolbert, S. H.; Smarsly, B. M.; Dunn, B.; Brezesinski, T. Pseudocapacitive Contributions to Charge Storage in Highly Ordered Mesoporous Group V Transition Metal Oxides with Iso-Oriented Layered Nanocrystalline Domains. *J. Am. Chem. Soc.* **2010**, *132*, 6982–6990.

71. Templin, M.; Franck, A.; Chesne, A. D.; Leist, H.; Zhang, Y.; Ulrich, R.; Schadler, V.; Wiesner, U. Organically Modified Aluminosilicate Mesostructures from Block Copolymer Phases. *Science* **1997**, *278*, 1795–1798.

72. Kuemmel, M.; Smatt, J.-H.; Boissiere, C.; Nicole, L.; Sanchez, C.; Linden, M.; Grosso, D. Hierarchical Inorganic Nanopatterning (INP) through Direct Easy Block-Copolymer Templating. *J. Mater. Chem.* **2009**, *19*, 3638–3642.

73. Baroch, P.; Hieda, J.; Saito, N.; Takai, O. Atmospheric Plasma-Calcination of Mesoporous Tungsten Oxide Utilizing Plasma Dielectric Barrier Discharge. *Thin Solid Films* **2007**, *515*, 4905–4908.

74. Maruo, T.; Tanaka, S.; Nishiyama, N.; Motoda, K.; Funayama, K.; Egashira, Y.; Ueyama, K. Low-Index Mesoporous Silica Films Modified with Trimethylethoxysilane. *Colloids Surf., A* **2008**, *318*, 84–87.

75. Besson, S.; Gacoin, T.; Jacquiod, C.; Ricolleau, C.; Babonneau, D.; Boilot, J.-P. Structural Study of 3D-Hexagonal Mesoporous Spin-Coated Sol−Gel Films. *J. Mater. Chem.* **2000**, *10*, 1331–1336.

76. Brezesinski, T.; Groenewolt, M.; Antonietti, M.; Smarsly, B. Crystal-to-Crystal Phase Transition in Self-Assembled Mesoporous Iron Oxide Films. *Angew. Chem., Int. Ed.* **2006**, *45*, 781–784.

77. Schleich, D. M.; Zhang, Y. Preparation of Some Metal Ferrite MFe$_2$O$_4$ Thin Films through a Nonaqueous Sol Method. *Mater. Res. Bull.* **1995**, *30*, 447–452.

78. Jiang, X.; Xie, Y.; Lu, J.; He, W.; Zhu, L.; Qian, Y. Preparation and Phase Transformation of Nanocrystalline Copper Sulfides (Cu$_9$S$_8$, Cu$_7$S$_4$ and CuS). *J. Mater. Chem.* **2000**, *10*, 2193–2196.

79. Chernyshova, I. V.; Hochella, M. F.; Madden, A. S. Size-Dependent Structural Transformations of Hematite Nanoparticles. 1. Phase Transition. *Phys. Chem. Chem. Phys.* **2007**, *9*, 1736–1750.

80. Baklanov, M. R.; Mogilnikov, K. P.; Polovinkin, V. G.; Dultsev, F. N. Determination of Pore Size Distribution in Thin Films by Ellipsometric Porosimetry. *J. Vac. Sci. Technol., B* **2000**, *18*, 1385–1391.

81. Gregg, S. J.; Sing, K. S. W. *Adsorption, Surface Area, and Porosity*, 2nd ed.; Academic: London, 1982.

82. Buonsanti, R.; Pick, T. E.; Krins, N.; Richardson, T. J.; Helms, B. A.; Milliron, D. J. Assembly of Ligand-Stripped Nanocrystals into Precisely Controlled Mesoporous Architectures. *Nano Lett.* **2012**, 10.1021/nl302206s.

83. Hillmyer, M. A.; Bates, F. S. Synthesis and Characterization of Model Polyalkane-Poly(ethylene oxide) Block Copolymers. *Macromolecules* **1996**, *29*, 6994–7002.

84. Allgaier, J.; Poppe, A.; Willner, L.; Richter, D. Synthesis and Characterization of Poly[1,4-isoprene-*b*-(ethylene oxide)] and Poly[ethylene-*co*-propylene-*b*-(ethylene oxide)] Block Copolymers. *Macromolecules* **1997**, *30*, 1582–1586.